Supporting Information

Barttfeld et al. 10.1073/pnas.1418031112

SI Materials and Methods

Propofol Anesthesia.

Administration. Monkeys were scanned in an awake resting condition and under two different levels of propofol sedation: moderate propofol sedation and deep propofol sedation (general anesthesia) defined by the monkey sedation scale (Table S1) and EEG. The monkeys were trained for i.v. propofol injection in the awake condition (5–7.5 mg/kg i.v.; Fresenius Kabi) in the saphenous vein for induction of sedation. Sedation was maintained using a target controlled infusion (TCI) system (Alaris PK Syringe pump; CareFusion) based on the Paedfusor pharmacokinetic model (1) for propofol. The TCI of propofol was 3.7–4.5 μg/mL for the moderate propofol sedation condition and 5.8–6.5 μg/mL for the deep propofol sedation condition. Muscle blocking agent (cisatracrium, 0.15 mg/kg bolus i.v., followed by continuous i.v. infusion at a rate of 0.18 mg/kg/h; GlaxoSmithKline) was used to avoid artifacts related to potential movements during moderate propofol sedation. Under sedation, all monkeys were intubated (Rüsch; Teleflex Medical; cuffed tube, internal diameter 4–4.5 mm) and mechanically ventilated (Aestiva/5 MRI; General Electric Healthcare) (tidal volume: 8–10 mL/kg; respiration rate of 23–31/min, end-tidal CO_2 of 40–42 mmHg, FiO_2 = 0.5). Physiological monitoring included heart rate, noninvasive blood pressure [systolic blood pressure, diastolic blood pressure, mean blood pressure, oxygen saturation (SpO_2), respiratory rate, end-tidal CO_2 ($EtCO_2$), cutaneous temperature]. All physiological parameters were recorded with a digital recording system (Maglife; Schiller). i.v. hydration was ensured by a mixture of normal saline (0.9%) and 5% glucose (250 mL of normal saline with 100 mL of 5% glucose) at a rate of 10 mL/kg/h. At the end of each fMRI scanning session, anesthesia was stopped, and the animal was monitored carefully during recovery. The animal was then placed in individual housing and monitored until full recovery from anesthesia.

Monitoring of anesthesia depth. We used both behavioral testing and EEG (see EEG methods below and Table S1) to define the anesthesia depth. The levels of arousal were defined using the Monkey Sedation scale, a clinical sedation scale that was adapted from the Human Observer's Assessment of Alertness/Sedation scale (2) and a previously described monkey arousal scale (3). At each fMRI session, the clinical score was determined at the beginning and the end of the scanning session. The clinical scale is based on spontaneous movements and the response to different stimuli (juice presentation, shaking/prodding, toe pinch) and corneal reflex (Table S1). In awake condition, monkeys scored positive in all items considered. Propofol monotonically caused negative responses to stimulation and spontaneous activity. Under moderate sedation, monkeys also stopped showing spontaneous movements while still tended to respond to shaking/prodding. Finally, under deep sedation monkeys stopped responding to all stimuli, reaching a state of general anesthesia.

EEG acquisition and analysis. We acquired EEG scalp recordings using a customized EEG cap (EasyCap, 13 channels), an MR amplifier (BrainAmp; Brain Products), and the Vision Recorder software (Brain Products). Parameters were as follow: sampling rate, 5,000 per channel; impedance, <20 MΩ; band-pass filtered 0.01 Hz < f < 500 Hz during collection. We applied an EEG gel to obtain low impedances (One Step EEG gel; Germany). To check the anesthesia level, EEG scalp recordings were acquired before entering the scanner room (10 min before starting MRI acquisition). We performed an online analysis through visual assessment of EEG traces. We interpreted the EEG traces visually and defined the EEG based levels of sedation for clinical sedative level (Table S1). Levels of sedation were defined as follow: level 1, awake condition, posterior alpha waves (eyes closed) and anterior beta waves; level 2, light propofol sedation, no fMRI data collection at this level, increasing of the amplitude of alpha waves and anterior diffusion of alpha waves; level 3, moderate propofol sedation, diffuse and wide alpha waves, and anterior theta waves (4); level 4, deep propofol sedation (general anesthesia), diffuse delta waves, waves of low amplitude (5, 6) and anterior alpha waves (10 Hz) (7); level 5, very deep sedation (deeper then level of general anesthesia), burst suppression (no fMRI data collection at this sedation level).

fMRI Data Acquisition. Monkeys were scanned on a 3-T horizontal scanner (Siemens Tim Trio) with a single transmit-receiver surface coil built in our institution and customized to monkeys. Each functional scan consisted of gradient-echoplanar whole-brain images (TR, 2,400 ms; TE, 20 ms; and 1.5-mm^3 voxel size; 500 brain volumes per session). For the awake condition, monkeys were implanted with an MR-compatible headpost and trained to sit in the sphinx position in a primate chair (8, 9). Monkeys sat in the dark inside the MRI without any task. The eye position was monitored at 120 Hz (Iscan Inc.). For the anesthesia sessions, animals were positioned in a sphinx position in the MR scanner and mechanically ventilated, and their physiological parameters were monitored. Seventy-seven sessions were performed, divided as follows: 21 awake sessions (monkey J: 16 sessions; monkey K: 5 sessions; monkey R: no awake session), 25 moderate propofol sedation sessions (monkey J: 2 sessions; monkey K: 11 sessions; monkey R: 12 sessions), and 31 deep propofol sedation sessions (monkey J: 9 sessions; monkey K: 10 sessions; monkey R: 12 sessions).

fMRI Preprocessing. Functional images were slice-time corrected, reoriented, realigned, and unwarped to correct for susceptibility-by-movement interaction, resampled (1-mm isotropic), rigidly coregistered to the anatomical template of the monkey MNI space (10), and smoothed (Gaussian kernel, 3-mm full width at half maximum) using FSL (www.fmrib.ox.ac.uk/fsl/) and custom Python code (8). We also removed by regression the movement parameters resulting from rigid body correction for head motion (11), as well as the global signal. We regressed out global signal from the images to rule out any confounding effect due to physiological (e.g., respiratory and cardiac) changes associated to propofol administration. Voxel time series were filtered with high-pass (0.0025-Hz cutoff) and low-pass (0.05 Hz cutoff) filters and with a zero-phase fast-Fourier (FFT) notch filter (0.03 Hz) to remove an artifactual pure frequency present in all sessions. Following a previous study (12), we normalized the variance of each time series; thus, covariance matrices correspond to correlation matrices.

Anatomical Dataset and Functional Atlas. Anatomical data were derived from the CoCoMac2.0 (13) database (cocomac.g-node.org) of axonal tract tracing studies using the Regional Map parcellation (14). This parcellation comprises 82 cortical ROIs (41 per hemisphere; Table S1). This anatomical connectivity matrix included interhemispheric connections. All connections were mirror-symmetrical across hemispheres. When information about the connectivity between two regions was not available in CoCoMac, the connection strength was set to 0 (15). The CoCoMac connectivity matrix classifies the strength of the

anatomical connections as weak, moderate or strong, codified as 1, 2, and 3, respectively. Following Shen et al. (15), when a description of strength was not provided, the connection strength was set to moderate.

The Regional Map parcellation was drawn on the F99 macaque standard cortical surface template (16, 17) and coregistered to the MNI space. Brain renders were done using custom Matlab scripts based on scripts by Gleg Begzin available at CoCoMac 2.0 webpage.

Stationary Connectivity Analysis. We estimated for each sedation condition c and session s the covariance matrix $C_{c,s}$, to confirm the presence of long-range stationary connections under awake and anesthesia (18, 19). To this aim, for each ROI, a time series was extracted for each session s, averaging all voxels within a ROI at a given brain volume. The matrix entry $C_{c,s}(i,j)$ indicates the temporal correlation of the average fMRI signal of ROIs i and j, which henceforth is referred as stationary functional connectivity. We estimated covariance from the regularized precision matrix (20). Following the graphical LASSO method (21), we placed a penalty on the L1 norm of the precision matrix to promote sparsity [the regularization parameter lambda (λ) was set to 0.1]. Through this method, we obtained a connectivity matrix per sedation condition and session, sized 82 × 82, which was Fisher transformed before further analysis as $z = ar\tanh(c)$ to obtain the $Z_{c,s}$, matrix.

Fig. 1*A* shows the average of this matrix, Z_c, one per sedation condition (Fig. 1*A*). To test for statistical significance of connectivity between brain regions in different sedation conditions, Student t tests were performed with the null hypothesis of zero correlation. To correct for the multiple comparisons, the false discovery rate (FDR) method was used, with a P value of 0.0001. To promote sparsity in the brain renders, we plotted into glass brains all significant connections that also displayed absolute connectivity strength higher than 0.3 (Fig. 1 *B–D*).

To characterize $Z_{c,s}$ matrices, we calculated for each sedation condition c and session s the average of positive z-values of $Z_{c,s}$ and also the rate between negative and positive z-values. We assessed significant differences between sedation conditions through a boostrapping method (22) as follows: we obtained for every sedation condition and session the mean value of all positive connection of every ROI, as

$$Z_{c,Positive} = \sum_{i=1}^{N} \frac{Zpos_{c,s}(i,j) \quad \text{if} \quad i \neq j}{N},$$

where $Zpos$ represents all z-values that are positive in a matrix $Z_{c,s}$ and N is the total number of positive z-values. After calculating $Z_{c,Positive}$, we subtracted the mean value of two condition (for instance, $Z_{awake,Positive} - Z_{deep,Positive}$), and called it the observed difference between conditions. We calculated the null distribution of $Z_{c,Positive}$ values differences between conditions shuffling scanning sessions across conditions (thus, breaking any possible dependence between sedation condition and connectivity value) and repeated the subtraction analysis 100,000 times, obtaining a distribution of random mean z-values differences that approaches a Gaussian distribution. This distribution is called null distribution and is the distribution of expected differences under the hypothesis of no relation between sedation condition and mean positive connectivity. If our observed difference in $Z_{c,Positive}$ is truly reflecting a difference between sedation conditions, its value should be located on a tail of the null distribution. We fitted a Gaussian to the null distribution to obtain a normalized $Z_{c,Positive}$, by subtracting to the observed $Z_{condition}$ the mean value of the fitted Gaussian and dividing it by the SD of the Gaussian distribution. We obtained the P value corresponding to the normalized $Z_{c,Positive}$ as the cumulative probability to the normalized observed difference in the normalized Gaussian distribution. This procedure was used each time a bootstrap analysis is performed in this work.

We also calculated for each condition c and each session s the rate of negative to positive z-values to quantify changes in negative z-values across conditions, as

$$rate_{c,s} = \frac{\sum_{i=1}^{N}\sum_{j=1}^{N} abs(Z_{i,j}) \,|\, Z_{i,j} < 0}{\sum_{i=1}^{N}\sum_{j=1}^{N} Z_{i,j} \,|\, Z_{i,j} > 0}.$$

Dynamical Connectivity Analysis.

Dynamical connectivity matrices. We estimated the sliding window covariance matrix $C_{c,s,w}$, for each sedation condition c, session s, and time window $w = 1....W$ (12). We computed covariance matrices from windowed segments of the time series. We used a Hamming window (width = 35 scans), sliding with steps of 1 scan, resulting in $W = 464$ windows per session. Because short time segments may have insufficient information to characterize the full covariance matrix, we estimated covariance from the regularized precision matrix (20). As done for the stationary analysis, we placed a penalty on the L1 norm of the precision matrix to promote sparsity (the regularization parameter λ was set to 0.1). This procedure resulted, for each condition c and session s, in a 3D matrix $C_{c,s,w}$ sized 82 × 82 × 464, which was Fisher transformed ($Z_{c,s,w}$) before further analysis.

Unsupervised clustering and brain states. To assess the structure of reoccurring connectivity patterns, we applied the k-means clustering algorithm (23) to $Z_{c,s,w}$ matrices, using the L1 distance function (Manhattan distance), as implemented in Matlab (MathWorks). Covariance values between all ROIs were included, resulting in $[82 \times (82-1)]/2 = 3{,}321$ features per matrix. Before clustering, $Z_{c,s,w}$ matrices were subsampled along the time dimension (w). Subsampling was performed to reduce redundancy between windows (12). The sampled connectivity matrices ($Zexamples_{c,s}$) were chosen as those windows with local maxima in functional connectivity variance (those peaks where the absolute normalized variance was higher than 0.5 SDs), resulting in 9.6 ± 2.54 (mean ± SD) windows or examples per session, for a total of 6,724 instances (samples from the $Z_{c,s,w}$ matrix). The clustering algorithm was applied to the $Zexamples_{c,s}$ and was repeated 500 times to increase chances of escaping local minima, with random initialization of centroid positions. The resulting centroids or median clusters (called BS_n with n = 1–7; each BS_n is sized 82 × 82) were then used to initialize a clustering of all data, i.e., not only the examples but the entire $Z_{c,s,w}$ matrices (77 fMRI sessions × 464 windows = 35,728 instances), obtaining a matrix of brain states $B_{c,s,w}$, which, for a given sedation condition c and session s, is a vector of length 464, valued 1–7 (the predefined number of clusters), because each matrix in $Z_{s,p,w}$ is assigned a BS_n. The number of clusters k (or brain states) was determined following ref. 12, although additional exploratory analyses varying k from 5 to 10 demonstrated consistent and robust results over a large range of k (Fig. S1).

Similarity score and probability of each state. To investigate the dependence of brain dynamics and sedation condition, we defined a measure of similarity between anatomical connectivity as provided by CoCoMac2.0 and functional connectivity, to rank all brain states along this dimension. The similarity score was computed by measuring the correlation coefficient between the vectorized structural matrix (sized 6,724 × 1) and each vectorized brain state or centroid from the clustering analysis (using the Euclidean distance instead of correlation or only positive values of the brain states to calculate the correlation, did not qualitatively changed the results; Fig. S3). Using the similarity score, we ranked all brain states in ascending order of similarity to structure (Fig. 2 *A* and *B*).

To calculate probability of occurrence of any brain state (Fig. 2*D*) we obtained, for each sedation condition c and each brain state n, the percentage of occurrence as

$$P_{c,n} = \frac{\sum_{i=1}^{N}(B_{c,s,i} = n)}{N},$$

in which $n = 464$. For each session, P_c adds up to 1. We calculated the SEM through a jackknife procedure (24), as follows: for each sedation condition c, we repeated the estimation of probability of occurrence for every brain state n ($P_{c,n}$), $N - 1$ times (N is the number of sessions within each sedation condition), each time excluding a different session from the analysis; SEM is then calculated as $sem_{c,x} = sqrt(P_{c,n}) * (N - 1)$.

To quantify the relation between probability of occurrence and similarity score, we conducted, for each sedation condition, a regression analysis, to quantify the beta value (β), the R^2, and a P value. Differences in brain state composition across vigilance conditions were assessed through a fixed-effects ANOVA, with mean rank similarity, that is, the result of averaging each brain state time series, valued from 1 (the less similar to structure brain state) to 7 (the more similar to structure brain state), as a dependent variable and the vigilance condition as the independent variable. We also run a fixed effects ANOVA to quantify the effect of sedation on the probability of brain state 7. For this, we followed the same procedure, but the mean rank similarity was calculated considering only the presence of brain state 7 (window w valued at 1) or any other state (window w valued at 0).

Topology and network properties of brain states. Fig. S2 shows several views of the brain states ordered according to their similarity score. Fig. S2*A* shows all connections, both positive and negative, above a threshold of z = 0.5. Fig. S2*B* shows the top 400 links of each brain state to explore the connectivity pattern dominating in each vigilance condition. We see that brain state 1 shows a clear characteristic pattern, with positive connections forming a frontoparietal core and negative connections showing long-range connections linking frontal and occipital regions. This pattern changes along the similarity axis, and brain state 7 presents a much more diffuse pattern, lacking a central core of positive connections. Fig. S2*C* shows the top 30 connected ROIs for each brain state. ROI size codifies the normalized number of connections. Fig. S2*D* shows the minimal energy plots of the brain states: using the Kamada–Kawai algorithm (25), we embedded the top 2,500 links of each brain state in the 2D plane. Resulting graphs show that networks are qualitatively different: brain states with low similarity score clearly show two subcomponents of the network, a subdivision that is completely lost in brain state 7 (despite having equal number of links; Fig. 2*D*).

Fig. 2*H* shows the normalized probability distribution of z-values for brain states 1 and 7, binning correlation values in 45 bins. Fig. 2 *I* and *J* shows the 2D normalized histograms of the same brain states z-values, as a function of distance between pairs of ROIs. Distance was between ROIs was calculated as the L2 norm in the 3D space, using MNI coordinates of CoCoMac as input.

Fig. 2*K* shows the four communities obtained from Shen et al. (15). For every brain state n, we calculated the absolute average correlation between all ROIs belonging to community i and all ROIs belonging to community j. To observe inter- and intracommunity mean correlation along the similarity axis, we conducted a regression, for every pair of communities, between the absolute value of correlation and the similarity score (Fig. 2*L*). We observe that, after Bonferroni correction, only correlations between communities 3 and 4 and between communities 3 and 1 significantly diminished as a function of similarity to structure. We set the P value at 0.05, Bonferroni corrected for multiple comparisons (10 possible community combinations). We also calculated for each brain state n the ratio intermodule vs. intramodule correlations, and we conducted a regression between this ratio and the similarity score (Fig. 2*M*).

We used a graph theory metric, Small World (SM) index, to summarize topological information (26, 27) (Fig. 2*N*). Each BS_n matrix defines a weighted graph where each ROI corresponds to a node and the weight of each link is determined by the z-value between each ROI pair. To calculate SM index, BS_n matrices were converted to binary undirected matrices by applying a threshold T. The arbitrary parameter T was chosen so that in all cases the resulting networks had a link density of 0.10, i.e., 10% of the total number of possible links in the networks were actually present, to ensure that only the strongest links are present but the network is not disaggregated into subcomponents (28) and to normalize networks of different brain states by size to avoid spurious effects on the metrics due to network size. On the thresholded matrices, we calculated the clustering coefficient C and the characteristic path length L using the Brain Connectivity Toolbox (27). Combining the metrics C and L, we calculated the SM index, as $SM = C/L$ (29). To quantify changes in SM across brain states, we conducted a regression analysis between the SM index and the similarity score.

We also quantified the duration of each brain state (that is, the average length of sequences of a given brain state in the $B_{c,s,w}$ matrix; Fig. 2*O*). For each sedation condition c and session s, we computed the length of sequences composed by only one brain state. To account for the random length duration, occurring solely due to a brain state's proportion (i.e., the more likely a brain state is, the longer its sequence is expected to be), we calculated a random distribution of sequence lengths by shuffling the $B_{c,s,w}$ 5,000 times along the time dimension. We then subtracted from the observed lengths the average time expected by frequency of each brain state. We quantified differences between sedation states through a bootstrap procedure, as done before.

To investigate putative changes in long-range temporal correlation (LRTC) and its relation with brain states, we estimated, for every session s, the Hurst exponent (H) through detrended fluctuation analysis (DFA) (30). DFA is a scaling analysis method that can be used in nonstationary time sequences. For each time series x of every session s, we subtracted its temporal mean and calculated its cumulative sum as

$$X_t = \sum_{i=1}^{t}(x_i - \langle x \rangle),$$

where $\langle x \rangle$ stands for the temporal mean of the signal. The cumulative signal X_t is divided into nonoverlapping windows of length 10 samples. A linear trend is fitted to this windowed time series using least squares, and then the signal is detrended by subtracting the best linear fit, producing signal Y_n. The root-mean-square deviation (that is, the fluctuation of the signal) is calculated from the detrended windowed time series, as

$$F_L = \sqrt{1/L \sum_{k=1}^{L} (Y_k - Y_n)^2}.$$

Finally, the Hurst exponent is obtained by plotting in a log-log graph F_L against L. Through least squares, we obtained the slope α of the relation between F_L and L. Because α changes for large values of F_L and L, we estimated α using the first 15 time windows (α_1). We identified the Hurst exponent with α.

Fig. S5*A* shows H values for each ROI within the Kotter and Wanke ROI set. Renders were done using custom scripts mentioned above. Fig. S5*B* shows H values for each session (averaged across brain regions). To construct Fig. S5*C*, we calculated for

each of the 77 functional sessions its average similarity score index that is the average value of the similarity score of all BS_n with n = 1–7, within a given session. Fig. S5*C* plots the H value for all 77 sessions as a function of the average similarity score (color codifies vigilance condition of each session). To construct Fig. S5*D*, we binned average similarity score into quintiles, averaging H values within each quintile. Error bar represents 1 SE, calculated using n = number of average brain values within each quintile.

To explore the possibility that the changes observed under sedation could be due to a slower brain dynamics, we conducted a lagged correlation analysis. For this, we repeated our analyses while introducing a time lag in the calculation of covariance between ROIs i and j. For this, we shifted one of the time series by either one or two samples relative to the other. In this way we obtained a lagged correlation value between ROIs i and j. We removed from the analysis the lagged correlation of a ROI with itself, yielding a value different from 1 when introducing a time lag. Fig. S6 shows these results. Fig. S6 *A* and *B* shows time-averaged connectivity matrices for all conditions, for lag = 0 (*a*), lag = 1 (*c*), and lag = 2 (*e*). To build those matrices, we averaged all temporal windows from the dynamical analysis. For lag 0 we obtained extremely similar results than using the graphical Lasso covariance calculation (Fig. S6 *A* and *B*; lag 0: awake: β-value = 0.36; R^2 = 0.13; P = 0.42; moderate: β-value = 0.53; R^2 = 0.91; P = 0.0008; deep: β-value = 0.422; R^2 = 0.82; P = 0.005). We found that introducing lags in the analysis did not affected our results, nor did it for lag 1 (Fig. S6 *C* and *D*; awake: β-value = 0.43; R^2 = 0.20; P = 0.30; moderate: β-value = 0.54; R^2 = 0.92; P = 0.0005; deep: β-value = 0.30; R^2 = 0.85; P = 0.0031) or for lag 2 (Fig. S6 *E* and *F*; awake: β-value = 0.51; R^2 = 0.39; P = 0.12; moderate: β-value = 0.47; R^2 = 0.87; P = 0.0018; deep: β-value = 0.40; R^2 = 0.84; P = 0.0037). Furthermore, the dynamical repertoire seemed to be even more depleted under sedation at larger lags, as brain state 7, the most dominant under sedation and closest to structural connectivity, became even more prominent during deep sedation as the lag increased from 0 to 2 (Fig. S6*G*).

To explore the robustness of our results, we also repeated the analysis using the inverse covariance matrix instead of the covariance matrix [as proposed by Allen et al. (12)]. We repeated our analysis using exactly the same methods and parameters than for covariance, mentioned above. It is known that sparsity-inducing norms such as the one used by the graphical Lasso model are not invariant under transformations such as translations and rotations (31). This invariance implies that distance similarities among covariance matrices are not necessarily translated into distance similarities among inverse covariance matrices. Nevertheless, we found that, although the results were noisier and less clear when using inverse covariance, they did not qualitatively change. We were able to reproduce the main findings: (*i*) modulation of brain state probability by similarity score (this time only in the deep sedation condition); (*ii*) strong reduction of negative links (i.e., restricting the analysis to covariance links whose inverse covariance value is different from zero) under sedation; and (*iii*) a shift of brain state probability as a function of sedation: in the awake condition, dominant states distant from structural connectivity are frequent, whereas under deep sedation, the brain states closest to anatomical structure dominate (Fig. S7*B*; β-value = 0.12; R^2 = 0.74; P = 0.01).

1. Absalom A, Kenny G (2005) 'Paedfusor' pharmacokinetic data set. *Br J Anaesth* 95(1):110.
2. Chernik DA, et al. (1990) Validity and reliability of the Observer's Assessment of Alertness/Sedation Scale: Study with intravenous midazolam. *J Clin Psychopharmacol* 10(4):244–251.
3. Vincent JL, et al. (2007) Intrinsic functional architecture in the anaesthetized monkey brain. *Nature* 447(7140):83–86.
4. Feshchenko VA, Veselis RA, Reinsel RA (2004) Propofol-induced alpha rhythm. *Neuropsychobiology* 50(3):257–266.
5. Murphy M, et al. (2011) Propofol anesthesia and sleep: A high-density EEG study. *Sleep* 34(3):283–91A.
6. Steriade M, Nuñez A, Amzica F (1993) A novel slow (< 1 Hz) oscillation of neocortical neurons in vivo: depolarizing and hyperpolarizing components. *J Neurosci* 13(8): 3252–3265.
7. Purdon PL, et al. (2013) Electroencephalogram signatures of loss and recovery of consciousness from propofol. *Proc Natl Acad Sci USA* 110(12):E1142–E1151.
8. Uhrig L, Dehaene S, Jarraya B (2014) A hierarchy of responses to auditory regularities in the macaque brain. *J Neurosci* 34(4):1127–1132.
9. Vanduffel W, et al. (2001) Visual motion processing investigated using contrast agent-enhanced fMRI in awake behaving monkeys. *Neuron* 32(4):565–577.
10. Frey S, et al. (2011) An MRI based average macaque monkey stereotaxic atlas and space (MNI monkey space). *Neuroimage* 55(4):1435–1442.
11. Fox MD, et al. (2005) The human brain is intrinsically organized into dynamic, anti-correlated functional networks. *Proc Natl Acad Sci USA* 102(27):9673–9678.
12. Allen EA, et al. (2014) Tracking whole-brain connectivity dynamics in the resting state. *Cereb Cortex* 24(3):663–676.
13. Bakker R, Wachtler T, Diesmann M (2012) CoCoMac 2.0 and the future of tract-tracing databases. *Front Neuroinform* 6:30.
14. Kötter R, Wanke E (2005) Mapping brains without coordinates. *Philos Trans R Soc Lond B Biol Sci* 360(1456):751–766.
15. Shen K, et al. (2012) Information processing architecture of functionally defined clusters in the macaque cortex. *J Neurosci* 32(48):17465–17476.
16. Bezgin G, Wanke E, Krumnack A, Kötter R (2008) Deducing logical relationships between spatially registered cortical parcellations under conditions of uncertainty. *Neural Netw* 21(8):1132–1145.
17. Van Essen DC, et al. (2001) An integrated software suite for surface-based analyses of cerebral cortex. *J Am Med Inform Assoc* 8(5):443–459.
18. Scholvinck ML, Maier A, Ye FQ, Duyn JH, Leopold DA (2010) Neural basis of global resting-state fMRI activity. *Proc Natl Acad Sci USA* 107(22):10238–10243.
19. Logothetis NK, et al. (2012) Hippocampal-cortical interaction during periods of subcortical silence. *Nature* 491(7425):547–553.
20. Varoquaux G, Gramfort A, Poline JB, Thirion B (2010) Brain covariance selection: Better individual functional connectivity models using population prior. *Advances in Neural Information Processing Systems*, eds Zemel R, Shawe-Taylor J. Curran Associates, Inc. (Vancouver), 2334–2342.
21. Friedman J, Hastie T, Tibshirani R (2008) Sparse inverse covariance estimation with the graphical lasso. *Biostatistics* 9(3):432–441.
22. Efron B, Tibshirani RJ (1994) *An Introduction to the Bootstrap* (Chapman and Hall, New York).
23. Lloyd S (1982) Least squares quantization in PCM. *IEEE Trans Inf Theory* 28(2):129–137.
24. Miller RG (1974) The jackknife—A review. *Biometrika* 61(1):1–15.
25. Kamada T, Kawai S (1989) An algorithm for drawing general undirected graphs. *Inf Process Lett* 31(1):7–15.
26. Sporns O, Zwi JD (2004) The small world of the cerebral cortex. *Neuroinformatics* 2(2): 145–162.
27. Rubinov M, Sporns O (2010) Complex network measures of brain connectivity: Uses and interpretations. *Neuroimage* 52(3):1059–1069.
28. Tagliazucchi E, von Wegner F, Morzelewski A, Brodbeck V, Laufs H (2012) Dynamic BOLD functional connectivity in humans and its electrophysiological correlates. *Front Hum Neurosci* 6(339):339.
29. Watts DJ, Strogatz SH (1998) Collective dynamics of 'small-world' networks. *Nature* 393(6684):440–442.
30. Peng CK, et al. (1992) Long-range correlations in nucleotide sequences. *Nature* 356(6365):168–170.
31. Yang J, Yu K, Huang T (2010) Supervised translation-invariant sparse coding. *IEEE Conference on Computer Vision and Pattern Recognition* (IEEE, San Francisco), pp 1–8.

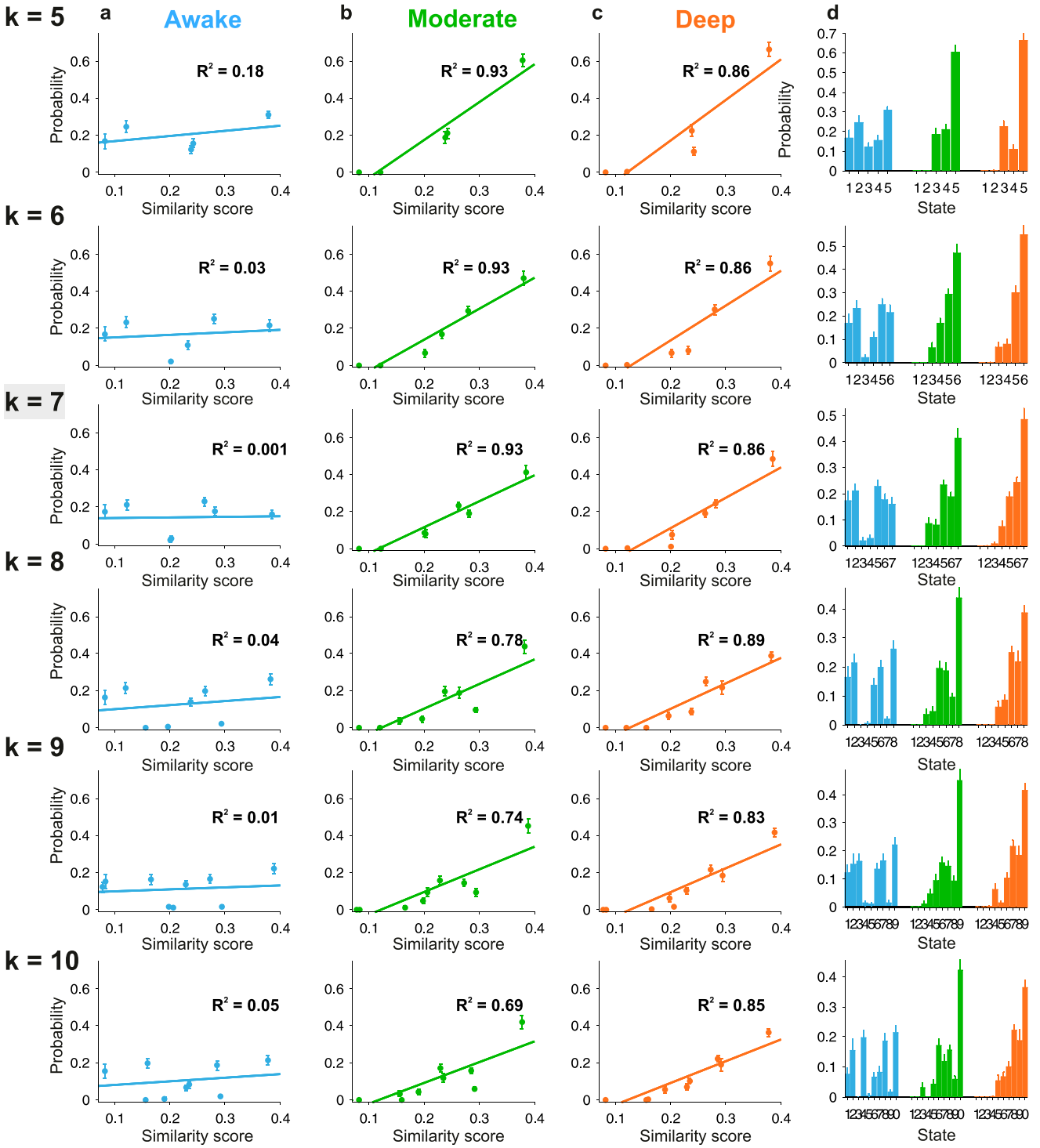

Fig. S1. Robustness of results with respect to the choice of a predefined number of brain states. To explore the dependence of results on the parameter k (number of predefined brain states), we explored a broad range of values for k = [5, 6, 7, 8, 9, 10] (main text only shows results for k = 7, highlighted in this figure). The relation between the probability of occurrence of a brain state and its similarity to the structural connectivity matrix for all sedation conditions (columns *A*–*C*) and the probability distributions (column *D*) do not significantly change with k.

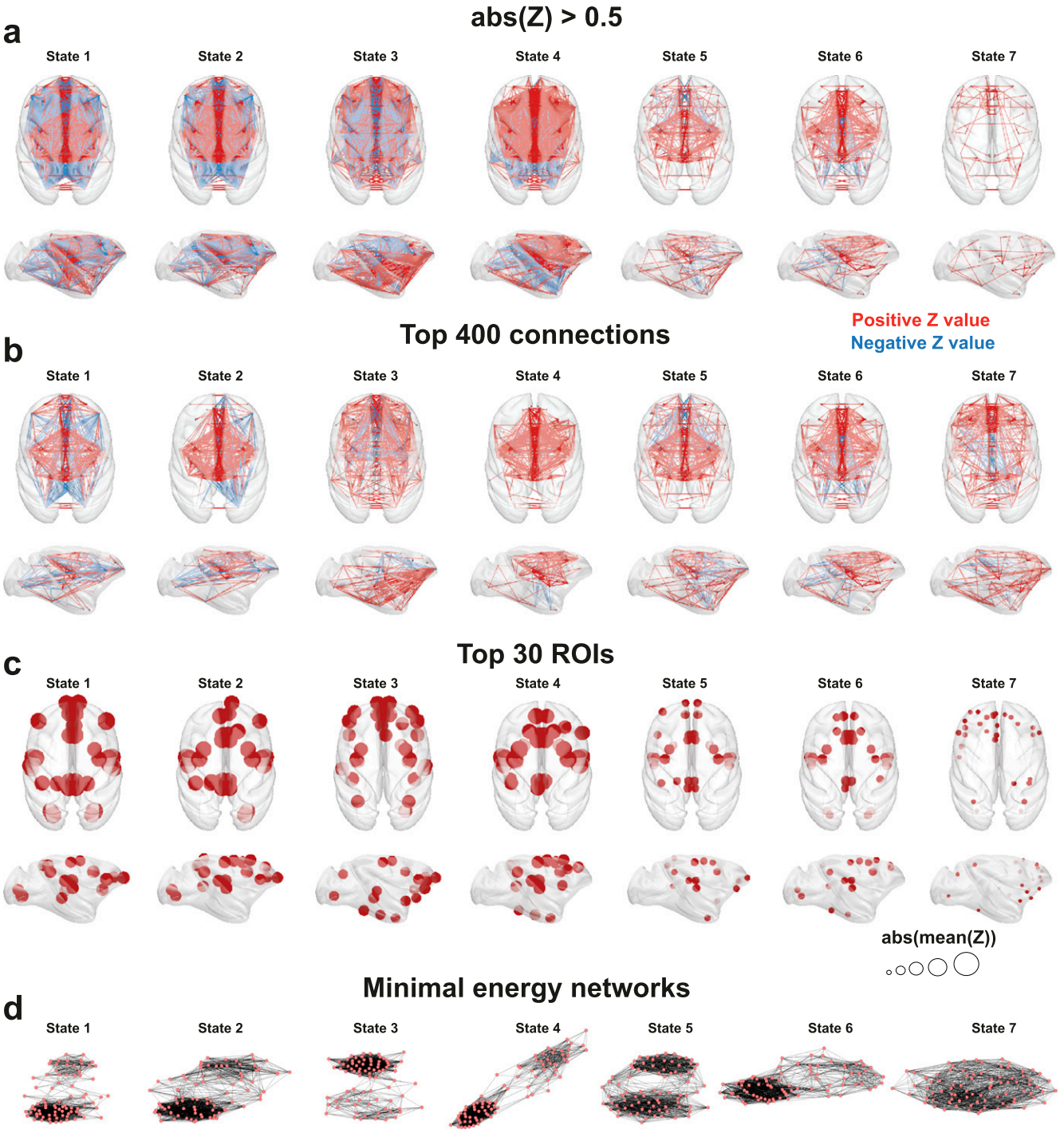

Fig. S2. Brain renders for the seven brain states, showing (*A*) the strongest connections (absolute z-value > 0.05), (*B*) the strongest 400 connections, (*C*) the top 30 more connected ROIs, and (*D*) the minimal energy plots embedded in two dimensions, displaying their strongest 2,500 links embedded in the plane.

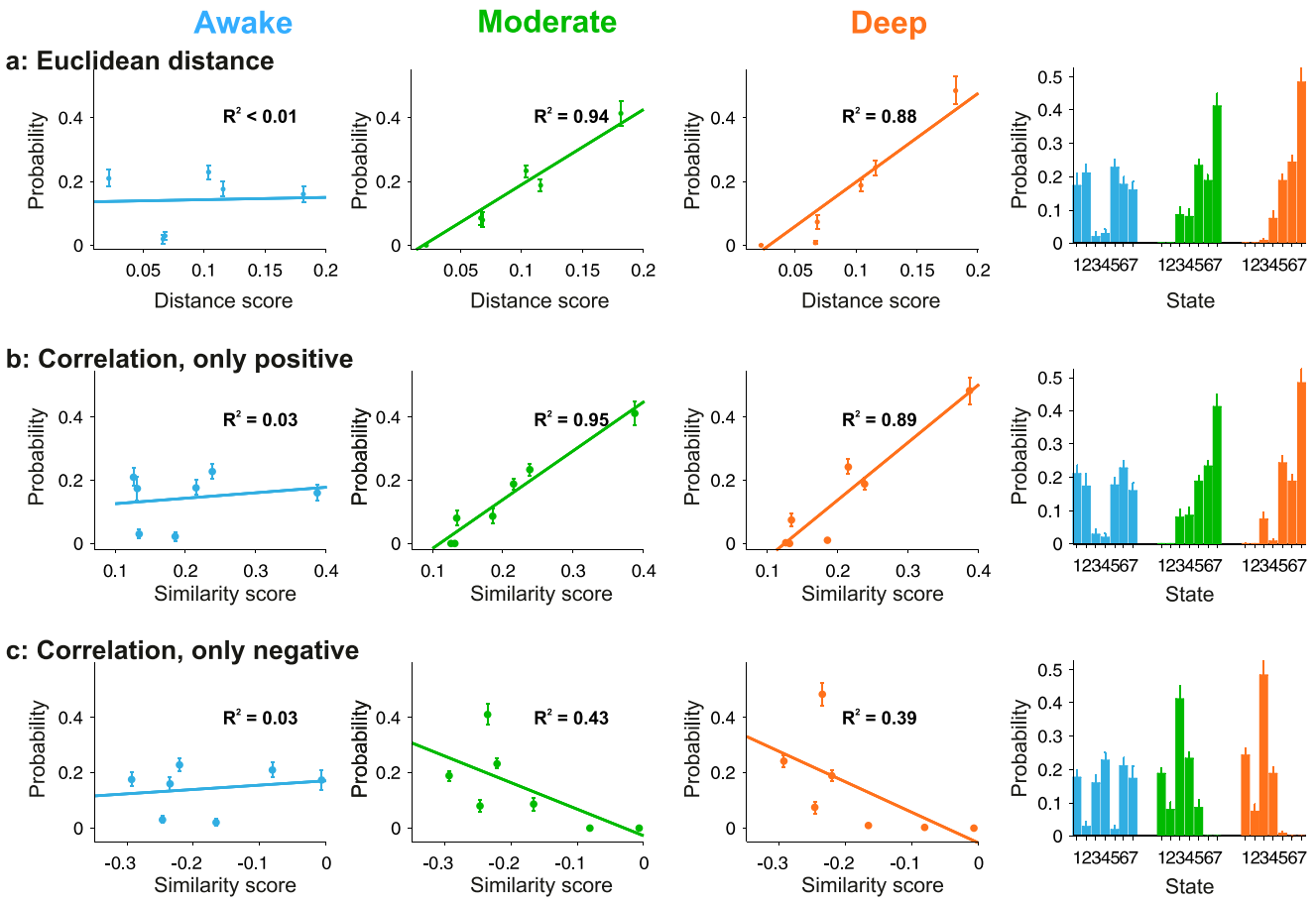

Fig. S3. Robustness of results with respect to alternative methods for evaluating the similarity between functional and anatomical networks. (*A*) Relation between probability of occurrence and similarity (*Left*) and probability distributions (*Right*) for a similarity score based on the Euclidean distance between brain state matrices and structural matrix. Probability of occurrence is plotted against the distance to anatomy (defined as 1 – similarity) to maintain the ascending slope on the curves for comparison. (*B*) Relation between probability of occurrence and similarity (*Left*) and probability distributions (*Right*) for a similarity calculated including only positive functional connectivity values (all negative values set to zero). (*C*) Same as above but including only negative correlations to calculate similarity (all positive correlations set to zero).

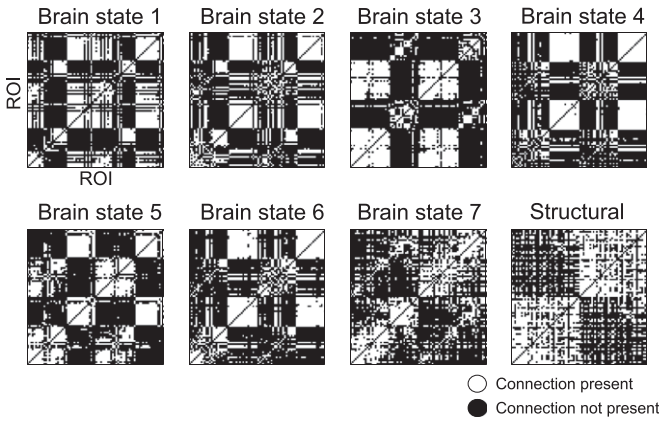

Fig. S4. Binarized correlation matrices showing only positive connections between ROIs for the anatomical matrix and the seven brain states. Brain states 1–6 display connectivity patterns that closely resemble the structure found in awake stationary analysis. In brain state 7, all structure is lost and positive connections spread all over the matrix, visually resembling the anatomical matrix.

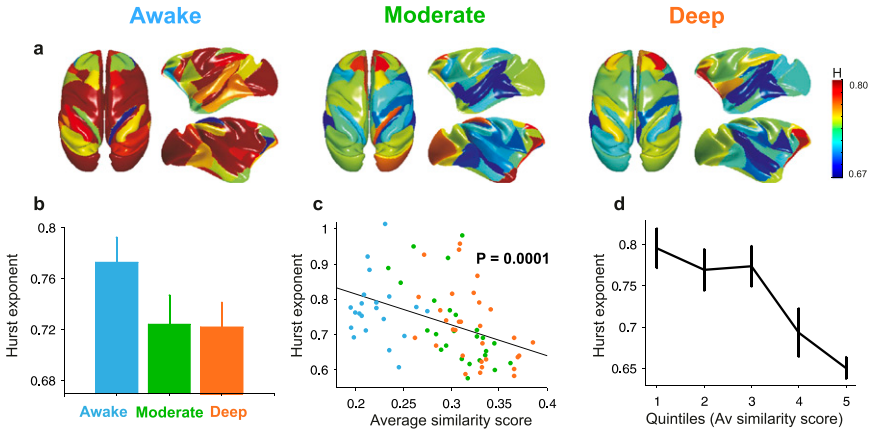

Fig. S5. Hurst exponent and its relation to brain states. (*A*) Hurst exponent value (*H*) for all sessions and ROIs. (*B*) *H* value for all three conditions, averaged across regions within each session. Error bars stand for SEM. (*C*) *H* value per session (for a total of 77 sessions) as a function of the mean similarity score. (*D*) *H* values grouped into quintiles of mean similarity score.

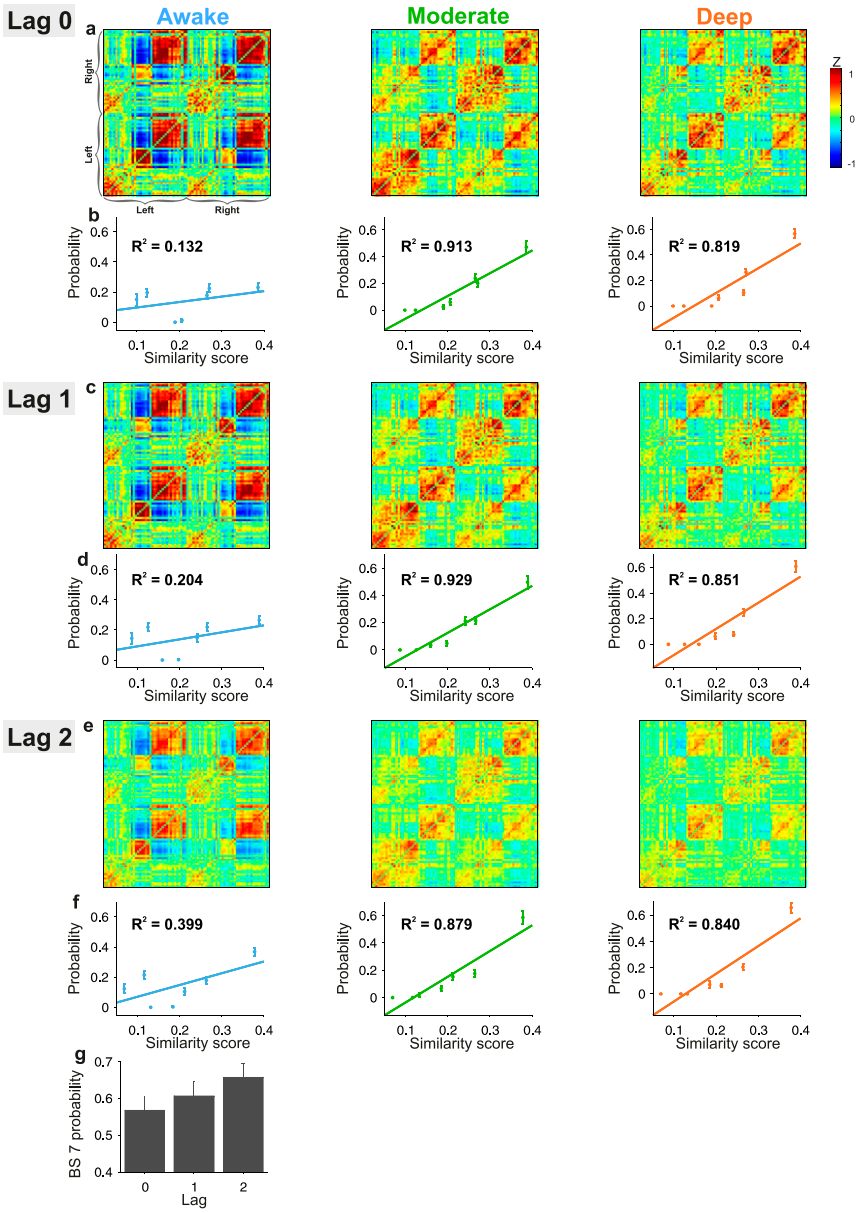

Fig. S6. Lagged-correlation analysis. (*A*, *C*, and *E*) Average connectivity matrices for all vigilance conditions, calculated by shifting the time series by zero (*A*), one (*C*), or two (*E*) fMRI samples (i.e., 0, 2.4, or 4.8 s). (*B*, *D*, and *F*) Probability of occurrence of each brain state as a function of the similarity between functional and structural connectivity for lag 0 (*B*), one (*D*), and two (*F*) conditions. (*G*) Probability of brain state 7, the dominant brain state under sedation, in deep anesthesia for lag = 0, 1, 2.

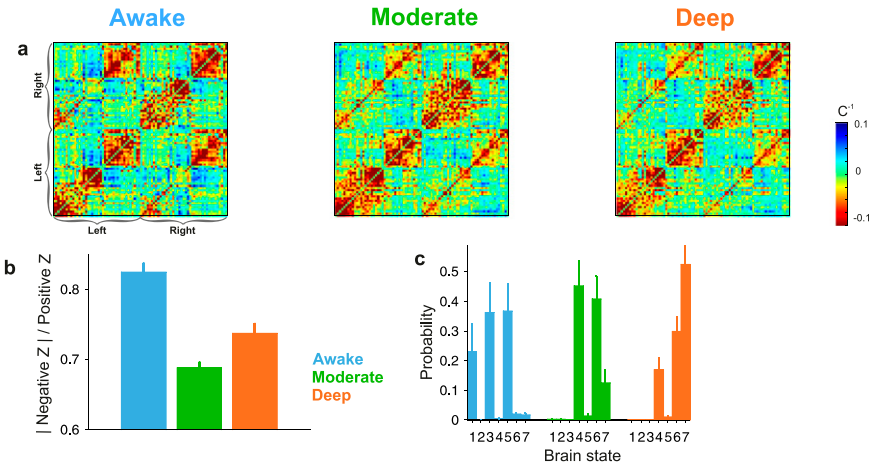

Fig. S7. Inverse covariance matrix and brain states. (*A*) Average inverse connectivity matrices for all vigilance conditions. Note that the color code is inverted for comparison with covariance matrices. (*B*) Rate between negative and positive covariance values considering only those connections that are different from zero in the corresponding inverse correlation matrix. (*C*) Probability distributions of brain states in the different vigilance conditions. Each bar represents the within-condition probability of occurrence of a state. Error bars stand for 1 SE.

Table S1. Monkey sedation scale

Scale	Arousal level	Juice presentation	Spontaneous movements	Shaking/prodding	Toe pinch	Corneal reflex
1	Awake	+	+	+	+	+
2	Moderate sedation	−	−	+/−	+	+
3	Deep sedation/general anesthesia	−	−	−	−	−

Juice presentation +, monkey reacts to juice presentation; spontaneous movements +, monkey moves spontaneously; shaking/prodding +, monkey has body movement, eye blinking, eye opening, or cardiac rate change during shaking/prodding; toe pinch +, monkey has body movement, eye blinking, eye opening, or cardiac rate change during toe pinching; corneal reflex +, monkey blinks eyes when cornea is stimulated.

Table S2. Functional brain atlas and community structure

Awake	Anterior cingulate, right
	Primary auditory, left
	Secondary somatosensory, right
	Primary auditory, right
	Anterior cingulate, left
	Secondary somatosensory, left
	Secondary auditory, right
	Posterior cingulate, left
	Posterior cingulate, right
	Primary somatosensory, right
	Ventrolateral prefrontal, right
	Secondary auditory, left
	Visual area 1, right
	Primary somatosensory, left
	Primary motor, right
Moderate sedation	Primary motor, left
	Primary motor, right
	Primary somatosensory, left
	Primary somatosensory, right
	Primary auditory, left
	Primary auditory, right
	Medial premotor, right
	Secondary somatosensory, left
	Anterior cingulate, right
	Medial premotor, left
	Anterior cingulate, left
	Secondary somatosensory, right
	Dorsomedial prefrontal, left
	Posterior cingulate, left
	Secondary auditory, right
Deep sedation	Medial premotor, left
	Anterior cingulate, left
	Primary auditory, left
	Anterior cingulate, right
	Secondary sensorimotor, left
	Medial premotor, right
	Primary sensorimotor, left
	Primary motor, left
	Secondary somatosensory, right
	Primary auditory, right
	Secondary auditory, right
	Dorsomedial prefrontal, left
	Posterior cingulate, left
	Secondary auditory, left
	Primary motor, right

Labels corresponding to the 82 ROIs of the Kotter and Wanke brain atlas and their module membership. Labels correspond to the ROIs in the left hemisphere; right hemisphere is equally ordered and has an almost equivalent module membership.

Table S3. Top 15 ROIs with the highest average absolute value covariance in the stationary analysis

ROI label	Module
Tempolar polar	1
Superior temporal	2
Amygdala	1
Orbito Inferior prefrontal	2
Anterior insula	2
Orbitomedial prefrontal	1
Central temporal	4
Orbitomedial prefrontal	1
Inferior temporal	4
Parahippocampal	4
Gustatory	2
Ventrolateral prefrontal	2
Anterior visual area	4
Posterior insula	2
Polar prefrontal	1
Hippocampus	4
Subgenual cingulate	1
Ventrolateral prefrontal	2
Visual area 2	4
Medial prefrontal	1
Ventral temporal	4
Dorsal anterior visual area	3
Visual area 1	4
Centrolateral prefrontal	1
Secondary auditory	2
Retrosplenial cingulate	4
Posterior cingulate	2
Anterior cingulate	1
Secondary somatosensory	2
Primary somatosensory	3
Primary auditory	2
Primary motor	3
Inferior parietal	3
Medial parietal	3
Dorsomedial prefrontal	1
Intraparietal	3
Superior parietal	3
Frontal eye field	3
Dorsolateral prefrontal	1
Medial premotor	3
Dorsolateral premotor	3

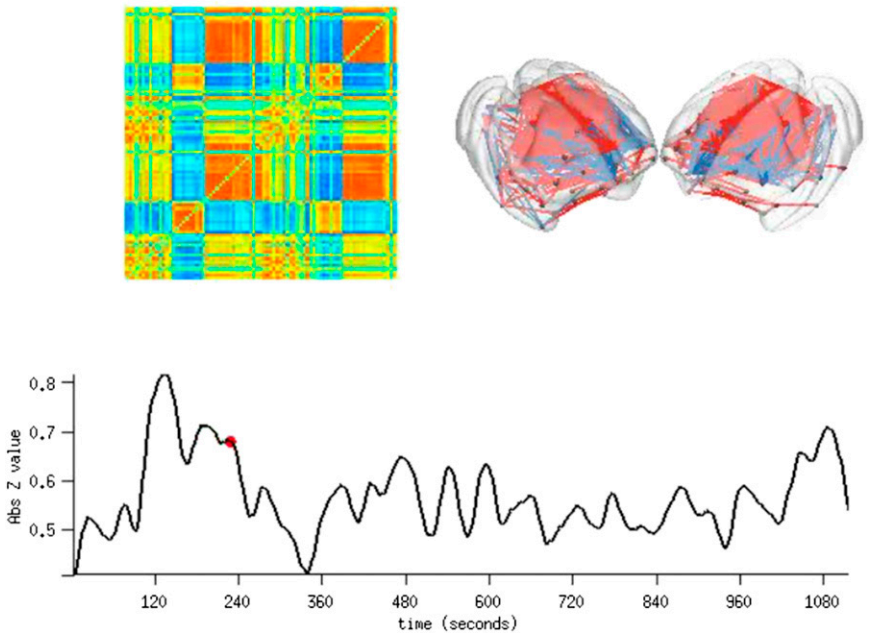

Movie S1. Dynamical connectivity matrix for the example fMRI session shown in Fig. 1*G*. Brain render shows the strongest connections (absolute z value higher than 1); red lines mark positive correlations, and blue lines mark negative correlations.

Movie S1